ChemSusChem

Research Article
doi.org/10.1002/cssc.202401872

**Chemistry
Europe**
European Chemical
Societies Publishing

www.chemsuschem.org

Self-Etching Synthesis of Superhydrophilic Iron-Rich Defect Heterostructure-Integrated Catalyst with Fast Oxygen Evolution Kinetics for Large-Current Water Splitting

Tingting Tang,[a] Yanfang Teng,[a] Kuoteng Sun,[c] Fengli Wei,[a] Luyan Shi,[a] Yongle Chen,[a] Sheraz Muhammad,[a] Tayirjan Taylor Isimjan,*[b] Jianniao Tian,*[a] and Xiulin Yang*[a]

Developing catalysts with rich metal defects, strong hydrophilicity, and extensive grain boundaries is crucial for enhancing the kinetics of electrocatalytic water oxidation and facilitating large-current water splitting. In this study, we utilized pH-controlled etching and gas-phase phosphating to synthesize a flower-like Ni_2P-FeP_4-Cu_3P modified nickel foam heterostructure catalyst. This catalyst features pronounced hydrophilicity and a high concentration of Fe defects. It exhibits low overpotentials of 156 mV and 210 mV at current densities of 10 and 100 mA cm^{-2} respectively, and maintains stability for up to 200 h at 100 mA cm^{-2} with only 7.3% degradation, showcasing outstanding electrocatalytic water oxidation performance. Fur-

thermore, when integrated into a Ni_2P-FeP_4-Cu_3P/NF||Pt–C/NF electrolyzer, it achieves excellent overall water splitting performance, reaching current densities of 10 and 400 mA cm^{-2} at just 1.47 V and 1.73 V, respectively, and operates stably for 60 h at 500 mA cm^{-2} with minimal degradation. Analysis indicates that high-valence oxyhydroxides/phosphides of Ni, Fe, and Cu act as the primary active species. The presence of abundant Fe defects enhances electron transfer, strong hydrophilicity improves electrolyte contact, and numerous grain boundaries synergistically modulate the activation energy between active sites and oxygen-containing intermediates, significantly improving the kinetics of water oxidation.

Introduction

To advance the objective of sustainable development, exploring clean and sustainable energy sources as alternatives to fossil fuels is crucial.[1] Hydrogen energy, recognized for its high energy density and environmental benefits, emerges as a compelling substitute.[3] Electrochemical water splitting is a viable method for hydrogen production, yet its efficiency is hampered by the anodic oxygen evolution reaction (OER). This reaction on the anode is inherently slow, involving complex steps like the formation of the O=O bond and multiple proton-coupled electron transfers, both of which present high energy barriers.[4] Despite the widespread use of Ir- and Ru-based materials in OER electrocatalysts, their scarcity, high cost, low current density, and limited durability present significant

challenges.[6] Consequently, research efforts have increasingly focused on developing efficient, cost-effective OER electrocatalysts that can achieve high current density ($>$400 mA cm^{-2}) while offering enhanced durability.[7]

In recent years, transition-metal phosphides (TMPs) have garnered attention due to their high catalytic activity, adjustable structure, stability, electrical conductivity, and composition.[8] A popular strategy to boost TMPs' intrinsic activity involves incorporating heteroatoms to modify their electronic structure.[10] Bimetallic or polymetallic phosphides often demonstrate enhanced electrochemical activity due to a synergistic effect among components. For example, $Fe_{0.29}Co_{0.71}P$ nanosheet arrays on nickel foam have shown outstanding OER performance as anodes for overall water splitting (OWS), thanks to an electron density modulation strategy.[12] Recent developments in heterostructured bimetallic phosphide, such as $(Ni_{0.33}Fe_{0.67})_2P$,[13] FeP/Ni_2P,[14] Ni_2P-Cu_3P,[15] Fe-CoP,[16] FeCo–P,[17] and NiCoP,[18] highlight their structural and performance benefits.

With insights into the OER process, TMP generally undergo dynamic self-reconstruction under oxidizing potentials to form metal oxides/(oxy)hydroxides, which exhibit significantly enhanced OER activity compared with directly synthesized oxide/(oxy)hydroxide counterparts.[19] Despite the advancement in TMP-based electrocatalysts for OER, their activity is still insufficient for industrial needs. Further improvement in catalytic performance can be achieved by modifying their morphological characteristics.[21] Grain boundary is a crystal defects that can introduce vacancies, dislocations, COFs-based metal-free heterojunctions[24] and bond distortions, affecting the coordination environment of nearby atoms and altering the

ChemSusChem

Research Article
doi.org/10.1002/cssc.202401872

Chemistry Europe
European Chemical
Societies Publishing

electronic structure of the active site. Integrating porous grain boundary catalysts with conductive substrates can adjust the electronic structure and create multiple new active sites, substantially boosting catalytic efficiency.[25] Moreover, vacancy defects have been proven beneficial in creating active sites and enhancing electrocatalytic activities, although their higher formation energy poses a challenge compared to anion vacancies.[27] Besides, the rate at which bubbles detach from the electrode surface and the electrode/electrolyte interface influences the mass transfer kinetics of generated gases and the catalytic efficiency of the catalyst. Hence, incorporating superhydrophilicity into the design of electrocatalysts represents an effective strategy for enhancing electrocatalytic performance.[29] The strategic engineering of multi-phase grain boundary in TMPs, combining various morphologies, grain boundary, vacancy defects, and surface hydrophilicity properties to enhance intrinsic activity, remains highly desirable.[30] Significant progress has been made in the development of electrolytic water-splitting catalysts over the past few decades.[31] However, most of these catalysts are tested under controlled laboratory conditions, typically at current densities below $100\ mA\,cm^{-2}$.[32] In contrast, industrial applications demand current densities ranging from 200 to $500\ mA\,cm^{-2}$. Therefore, it is crucial to focus research on designing catalysts that can perform effectively under high-current conditions.[33]

Herein, we present a flower-like Fe defect-rich Ni_2P-FeP_4-Cu_3P/NF catalyst developed through pH regulation and gas-

phase phosphorization, which displays superhydrophilicity and abundant grain boundaries. Characterization confirmed its flower-like structure with a larger specific surface area, potentially exposing more active sites. Superhydrophilicity was verified by contact angle tests, abundant Fe defects by electron paramagnetic resonance, and numerous grain boundaries by transmission electron microscopy. Electrochemical assessments showed that this catalyst requires only 156 and 210 mV overpotentials to achieve current densities of 10 and $100\ mA\,cm^{-2}$, respectively, in a 1.0 M KOH electrolyte. Furthermore, it achieved a cell voltage of 1.47 V at $10\ mA\,cm^{-2}$ during overall water splitting, surpassing the benchmark $RuO_2 \| Pt/C$ (1.53 V), and maintained stability for over 60 h at $500\ mA\,cm^{-2}$. In situ characterization reveals that partial metal phosphides convert to hydroxide oxides at higher potentials, which, along with residual metal phosphides, serve as active species to lower the activation energy of oxygen-containing intermediates, thereby enhancing water oxidation kinetics.

Results and Discussion

Synthesis and Characterizations

The synthesis of flower-like Ni_2P-FeP_4-Cu_3P/NF catalyst is depicted in Figure 1a. This study employed a pH-controlled one-step hydrothermal method to synthesize NiFeCu/NF pre-

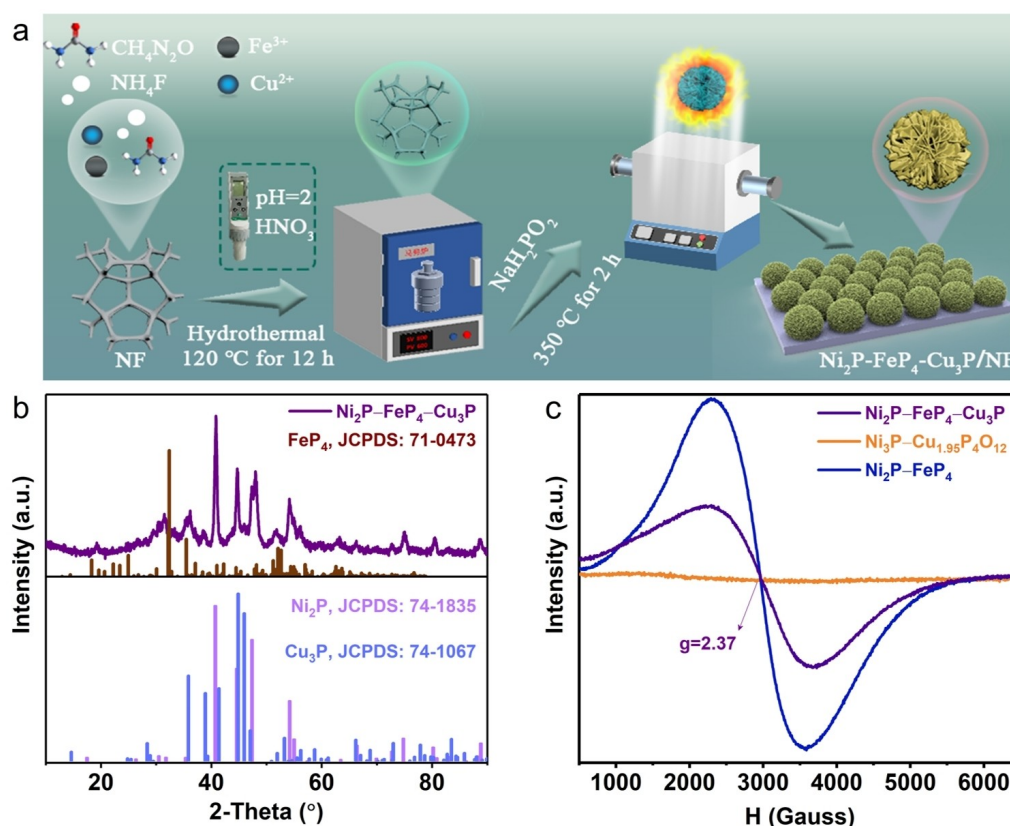**Figure 1.** (a) Schematic illustration of the preparation of the Ni_2P-FeP_4-Cu_3P/NF. (b) XRD pattern of Ni_2P-FeP_4-Cu_3P/NF. (c) EPR spectra of Ni_2P-FeP_4-Cu_3P/NF, Ni_2P-FeP_4/NF, and Ni_3P-$Cu_{1.95}P_4O_{12}/NF$.

cursor, which was subsequently transformed through gas-phase phosphorization to create a flower-like Ni_2P-FeP_4-Cu_3P/NF target catalyst. The crystal structure of the catalyst was examined using X-ray diffraction (XRD). The XRD pattern shows that the Ni_2P-FeP_4-Cu_3P/NF catalyst comprises crystalline phases of FeP_4 (JCPDS: 71–0473), Ni_2P (JCPDS: 74–1835), and Cu_3P (JCPDS: 74–1067) as illustrated in Figure 1b. In comparison, the precursor compounds of NF loaded with only Fe and Cu underwent phosphatization and transformed into Ni_2P-FeP_4/NF and Ni_3P-$Cu_{1.95}P_4O_{12}$/NF, respectively (Figure S2a and b). The Raman spectra of Ni_2P-FeP_4-Cu_3P/NF, shown in Figure S3, reveal four significant peaks at 180, 417, 463, and 1636 cm^{-1}, which correspond to the vibrational modes of Cu_2O,[35] NiO, α-Ni(OH)$_2$, and O−H bending mode of H_2O,[36] respectively. Additionally, the type and concentration of defects were assessed by analyzing horizontal and vertical differences in the electron paramagnetic resonance (EPR) spectra. In the EPR spectra, both Ni_2P-FeP_4-Cu_3P/NF and Ni_2P-FeP_4/NF exhibited a similar signal around g = 2.37 (Figure 1c), attributed to electrons trapped in Fe defects.[38] Ni_2P-FeP_4/NF showed the highest signal intensity, indicating a greater concentration of defects.[39] It is important to note that the presence of moderate Fe defects in the target catalyst is critical for facilitating electron transfer and enhancing the reaction kinetics.[41]

To examine the morphology of the prepared sample, both scanning electron microscopy (SEM) and transmission electron microscopy (TEM) were utilized. As shown in Figures 2a and S4, the Ni_2P-FeP_4-Cu_3P/NF retains its initial flower-like structure post-phosphorization, suggesting that the gas-phase phosphating process does not alter the morphology of the Ni_2P-FeP_4-Cu_3P formed in situ on the NF surface. In contrast, Ni_3P-$Cu_{1.95}P_4O_{12}$/NF exhibits a distinct blocky-shaped particle formation, densely distributed and anchored on NF (Figure S5a). Ni_2P-FeP_4/NF presents an inhomogeneous structure that includes nanosheets and a flower-like formation (Figure S5b), whereas Ni_2P/NF consists of nanorods (Figure S5c). The microsheet structures of Ni_2P-FeP_4-Cu_3P/NF−X (X = 0.2, 0.4, 0.8, and 1.0) synthesized using solutions with varying concentrations of $Cu(NO_3)_2$ (0.2, 0.4, 0.8, and 1.0 mmol, respectively) exhibit subtle differences (Figure S6a–d). It is also noteworthy that the microsheet structures of Ni_2P-FeP_4-Cu_3P/NF-pH (pH = 1, 3, 4, and 5) display distinct variations (Figure S7a–d). As the pH of the solution increases, notably beyond a threshold of 3, the thickness of the nanosheet layers also increases. These morphological changes arise from variations in $Cu(NO_3)_2$ concentration and pH, which lead to increased copper ion concentrations in the solution. This, in turn, impacts the chemical and physical behavior of copper within the catalyst, causing changes in
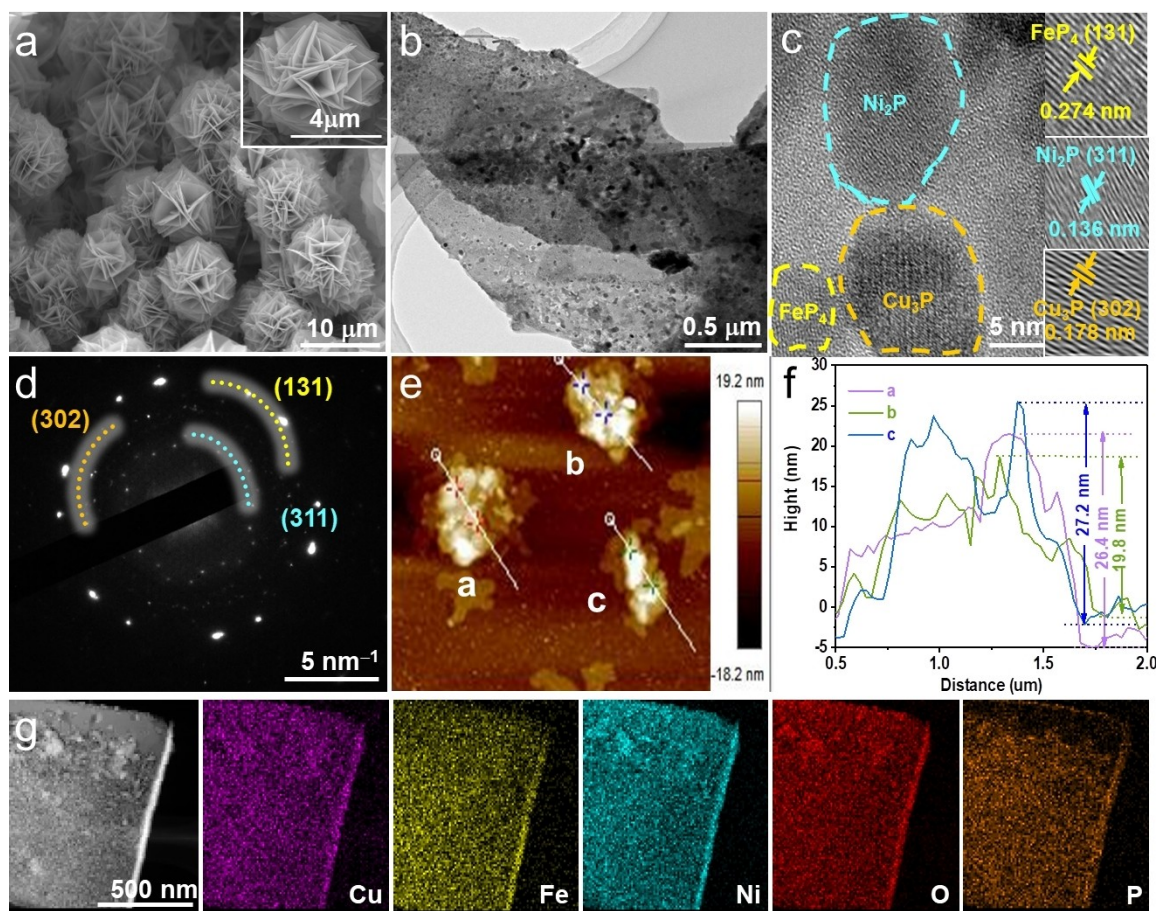

Figure 2. (a) SEM image, (b) TEM image, (c) HRTEM image, (d) SAED pattern, (e) AFM image, (f) corresponding height profiles and (g) HAADFSTEM image with corresponding elemental mappings of the Ni_2P-FeP_4-Cu_3P/NF.

crystallinity, phase, morphology, pore structure, and surface elemental states. These alterations collectively influence both the morphology and performance of the catalyst.[42] The optimal synthesis conditions were found using a solution with a pH of 2 and a $Cu(NO_3)_2$ concentration of 0.6 mmol, which not only improved the structural complexity but also significantly enhanced the number of active sites on the catalyst. The TEM image confirms that there are abundant particulate materials on the surface of the nanosheets (Figure 2b), and this rough surface facilitates the presentation of more active sites. Atomic force microscopy (AFM) measurements, as depicted in Figure 2e and f, reveal that the average thickness of the Ni_2P-FeP_4-Cu_3P/ NF nanoflake layer is approximately 24.4 nm. The high-resolution TEM (HRTEM) image in Figure 2c shows numerous dispersed amorphous areas alongside crystalline regions with varying orientations, highlighting a coexistence of crystalline and amorphous heterointerfaces. In these crystalline regions, Ni_2P, FeP_4, and Cu_3P coexist, identified by lattice spacings of 0.136 nm (Ni_2P (311) plane), 0.274 nm (FeP_4 (131) plane), and 0.178 nm (Cu_3P (302) plane), suggesting that these phases are in close contact, forming distinct heterojunction interfaces that usually expose numerous active centers. The multiphase nature of the flower-like structure is further verified by selected area electron diffraction (SAED, Figure 2d).[46] Additionally, the energy-dispersive X-ray (EDX) spectrum (Figure S8) and elemental mapping images (Figure 2g) confirm a uniform distribution of Cu, Fe, Ni, O, and P elements within the flower-like structure of Ni_2P-FeP_4-Cu_3P/NF.

To explore the surface chemical composition and valence states of different catalysts, X-ray photoelectron spectroscopy (XPS) was performed. The XPS survey spectra of Ni_2P-FeP_4-Cu_3P/ NF revealed distinct signals corresponding to the Ni, P, Cu, and Fe elements (red curve in Figure S9), aligning with XRD and EDX analysis results. The high-resolution C 1s spectrum (Figure S10) served as a reference for correcting other elements. In the high-resolution XPS spectra of Ni $2p_{3/2}$ (Figure 3a), peaks at 853.3 eV correspond to the Ni–P bond in both Ni_2P-FeP_4-Cu_3P/ NF and Ni_2P-FeP_4/NF. Additional peaks at 856.6 and 858.3 eV are attributed to Ni^{2+} and Ni^{3+}, respectively, with satellite peaks at 860.9 and 863.5 eV.[47] The Ni–P bond in Ni_2P-FeP_4-Cu_3P/NF exhibits a positive shift of 0.5 eV compared to Ni_3P-$Cu_{1.95}P_4O_{12}$/ NF, indicating a strong electronic interaction between Fe and Ni species.[20] Figure 3b shows that peaks at 706.9 eV primarily originate from the Fe–P bond in Ni_2P-FeP_4-Cu_3P/NF, with Fe^{2+}/ Fe^{3+} peaks and a satellite peak observed at 710.9, 714.1 eV, and 717.7 eV, respectively.[49] Compared to Ni_2P-FeP_4/NF, the Fe–P bond in Ni_2P-FeP_4-Cu_3P/NF shifts towards a higher binding energy by 0.30 eV.[20, 23] This shift indicates increased oxidation states of Ni and Fe cations, enhancing oxygen evolution reaction (OER) performance. The enhancement results from the doping of electronegative Cu, which modifies the electronegativity of P anions, increasing electron attraction to Ni and Fe, thereby raising their oxidation states and altering the surrounding electron density.[50] Additionally, a lower Fe^{2+}/Fe^{3+} peak area ratio (1.09) in Ni_2P-FeP_4-Cu_3P/NF compared to Ni_2P-FeP_4/NF (1.17) suggests a high density of Fe defects in the target catalyst.[40, 52] The deconvoluted Cu 2p spectrum shown in Figure 3c exhibits peaks at 932.8/952.5 eV, attributed to the Cu $2p_{3/2}$ and Cu $2p_{1/2}$ states of Cu^+, respectively, and peaks at 934.9/954.6 eV for Cu^{2+}. Two satellite peaks at 942.0/963.3 eV
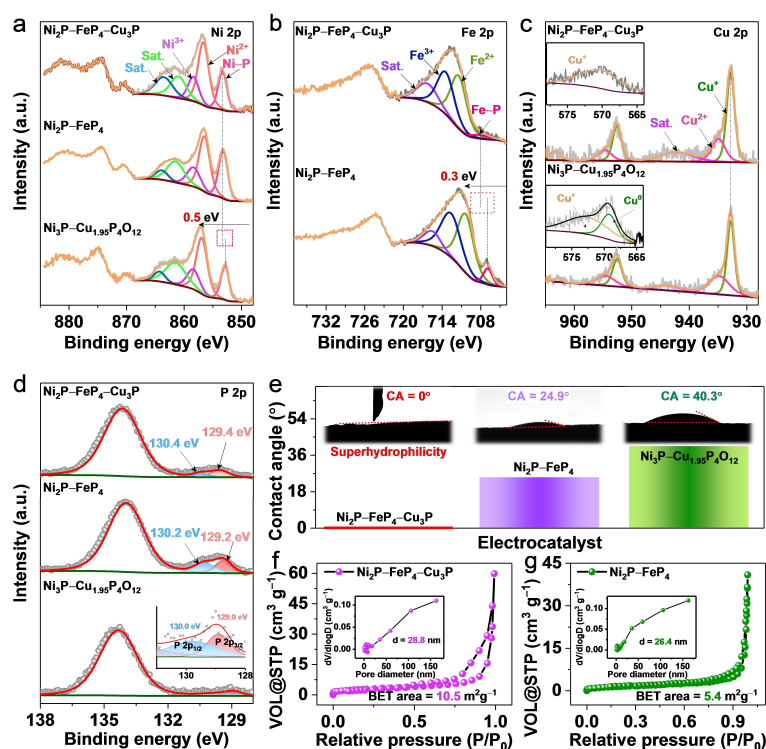

Figure 3. High resolution XPS spectra of (a) Ni 2p, (b) Fe 2p, (c) Cu 2p, and (d) P 2p of designed catalysts. (e) Contact angles of comparable catalysts. N_2 adsorption/desorption isotherms and pore size distributions (inset) of (f) Ni_2P-FeP_4-Cu_3P/NF and (g) Ni_2P-FeP_4/NF.

ChemSusChem

Research Article
doi.org/10.1002/cssc.202401872

Chemistry Europe
European Chemical
Societies Publishing

correspond to Cu $2p_{3/2}$ and Cu $2p_{1/2}$, respectively.[53] A detailed analysis utilizing the Cu LMM Auger peak (inset of Figure 3c) identifies a prominent component at 570.4 eV, attributed to Cu^+ species, confirming the presence of exclusively Cu^+ in $Ni_2P-FeP_4-Cu_3P/N$. In contrast, the $Ni_3P-Cu_{1.95}P_4O_{12}/NF$ catalyst exhibits two distinct valence states, Cu^0/Cu^+, aligning with XRD findings.[56]

The high-resolution XPS spectra of P 2p in $Ni_2P-FeP_4-Cu_3P/$ NF, shown in Figure 3d, reveal P $2p_{3/2}$ at 129.4 eV, P $2p_{1/2}$ at 130.4 eV, and P—O species at 134.1 eV on the surface. The binding energy of P—M (P 2p) bonds varies among catalysts, with the targeted catalyst exhibiting a slight positive shift, indicating strong interactions between metal atoms and P atoms.[49, 57] This shift leads to enhanced local electric dipoles, which are beneficial for H_2O adsorption and weakening of the H—O bonds in adsorbed H_2O, thereby improving reaction kinetics.[58]

The surface wettability of the fabricated electrodes was evaluated through contact angle measurements. The $Ni_2P-FeP_4-Cu_3P/NF$ electrode shows superhydrophilic properties (Figure 3e), as water droplets immediately permeate the electrode surface, reducing the static contact angle to zero. In contrast, water contact angles on Ni_2P-FeP_4/NF and $Ni_3P-Cu_{1.95}P_4O_{12}/NF$ were 24.9° and 40.3°, respectively. The flower-like structure of $Ni_2P-FeP_4-Cu_3P/NF$ provides a high specific surface area that enhances its superhydrophilicity. This improvement is attributed to the increased surface roughness, which results from the dense distribution of small mesopores across its large surface area, thereby significantly improving surface wettability.[59] This superhydrophilicity facilitates close electrolyte-electrode contact and rapid electrolyte diffusion, enhancing mass and charge transfer and accelerating reaction kinetics.[14, 61] Brunauer-Emmett-Teller (BET) analysis of $Ni_2P-FeP_4-Cu_3P/NF$ and Ni_2P-FeP_4/NF catalysts, shown in Figure 3f and g exhibits typical type III isotherms with mesoporous characteristics and distinct hysteresis loops.[63] $Ni_2P-FeP_4-Cu_3P/NF$ displays a higher BET surface area (10.5 $m^2 g^{-1}$) than Ni_2P-FeP_4/NF (5.4 $m^2 g^{-1}$), which helps expose more active sites, facilitates electrolyte diffusion, and improves gas emissions.[65]

Electrocatalytic Performance

The OER performance of the catalysts was meticulously evaluated using a standard three-electrode setup in a 1.0 M KOH solution. All potentials were corrected for 100% iR and calibrated against the reversible hydrogen electrode (RHE, Figure S1). Notably, the $Ni_2P-FeP_4-Cu_3P$ catalyst demonstrated exceptional catalytic performance under optimized conditions, achieved by adjusting the pH of the solution to 2 and the $Cu(NO_3)_2$ concentration to 0.6 mmol (Figures S12–S15). All subsequent discussions and analyses will focus on these optimal synthesis conditions.

As depicted in Figure 4a, the $Ni_2P-FeP_4-Cu_3P/NF$ requires only 156 and 210 mV overpotentials to reach current densities of 10 and 100 $mA cm^{-2}$, respectively. These values are significantly lower than those required by $Ni_3P-Cu_{1.95}P_4O_{12}/NF$

(208 mV, 293 mV), Ni_2P-FeP_4/NF (184 mV, 241 mV), Ni_2P (160 mV, 338 mV), and RuO_2 (220 mV, 352 mV). Furthermore, the $Ni_2P-FeP_4-Cu_3P/NF$ delivered an ultra-low overpotential of 211 mV at 100 $mA cm^{-2}$, outperforming all other tested electrocatalysts (Figure 4c). The OER performance of $Ni_2P-FeP_4-Cu_3P/NF$ was also tested under various pH levels and Cu contents, with the findings indicating the lowest overpotential under the optimized conditions.

The superior OER performance is attributed to the unique flower-like structure of the catalyst, which facilitates electrolyte diffusion and enhances the synergistic effects of Ni, Fe, and Cu phosphorylation, thereby exposing numerous active sites.[66] Tafel slopes calculated from linear sweep voltammetry (LSV) data indicate that $Ni_2P-FeP_4-Cu_3P/NF$ has a Tafel slope of approximately 43.6 $mV dec^{-1}$ (Figure 4b), significantly lower than those of its counterparts. This suggests faster reaction dynamics than other catalysts such as $Ni_3P-Cu_{1.95}P_4O_{12}/NF$, Ni_2P-FeP_4/NF, and RuO_2 on nickel substrate. $Ni_2P-FeP_4-Cu_3P/NF$ similarly outperforms recent non-precious metal catalysts in OER overpotential and Tafel slope, as shown in Figure 4d and Table S1. The electrochemical double-layer capacitance (C_{dl}) was measured through cyclic voltammetry (CV) in the non-Faradaic region at various scan rates (Figure S11).[67] $Ni_2P-FeP_4-Cu_3P/NF$ exhibited a C_{dl} of 134.0 $mF cm^{-2}$, significantly higher than those of $Ni_3P-Cu_{1.95}P_4O_{12}/NF$, Ni_2P-FeP_4/NF, Ni_2P/NF, and RuO_2/NF (Figure 4e). This high C_{dl} indicates an electrochemical surface area (ECSA) of 3350 cm^2 for $Ni_2P-FeP_4-Cu_3P/NF$, surpassing those of its competitors (Figure 4f), suggesting more active sites and enhanced catalytic performance.[68] Nyquist plots further demonstrate minimal charge transfer resistance (R_{ct}) for $Ni_2P-FeP_4-Cu_3P/NF$ compared to other catalysts, indicating rapid charge transfer across the electrode-electrolyte interface and faster kinetics for OER (Figure 4g, S12d and S14d).[69] Durability tests also revealed robust long-term stability, with only a 7.3% decline in current density after 200 h at a constant current density of 100 $mA cm^{-2}$ (Figure 4h). The initial decline during the first 80 h, likely due to solution replenishment, was followed by gradual stabilization. Furthermore, it demonstrated robust stability during the OER stability test conducted at industrial-level current densities of 500 $mA cm^{-2}$. Further stability tests through multi-cycle CV indicated a negligible shift in polarization curves after 1000 and 7000 CV cycles (inset Figure 4h), underscoring the catalyst's durability. The slight decrease in catalytic performance is primarily attributed to catalyst aggregation, exfoliation, and changes in the surface chemical state (Figure 6c–f), emphasizing the robustness and potential practical applications of $Ni_2P-FeP_4-Cu_3P/NF$ in OER processes.

Overall Water Splitting Performance

Leveraging the remarkable OER performance demonstrated by the as-synthesized $Ni_2P-FeP_4-Cu_3P/NF$ in alkaline electrolytes, where it served as the anode paired with commercial Pt/C as the cathode, the overall water electrolysis performance was evaluated using a symmetrical two-electrode system (Figure 5a). To achieve a current density of 10 $MA cm^{-2}$ in 1.0 M KOH
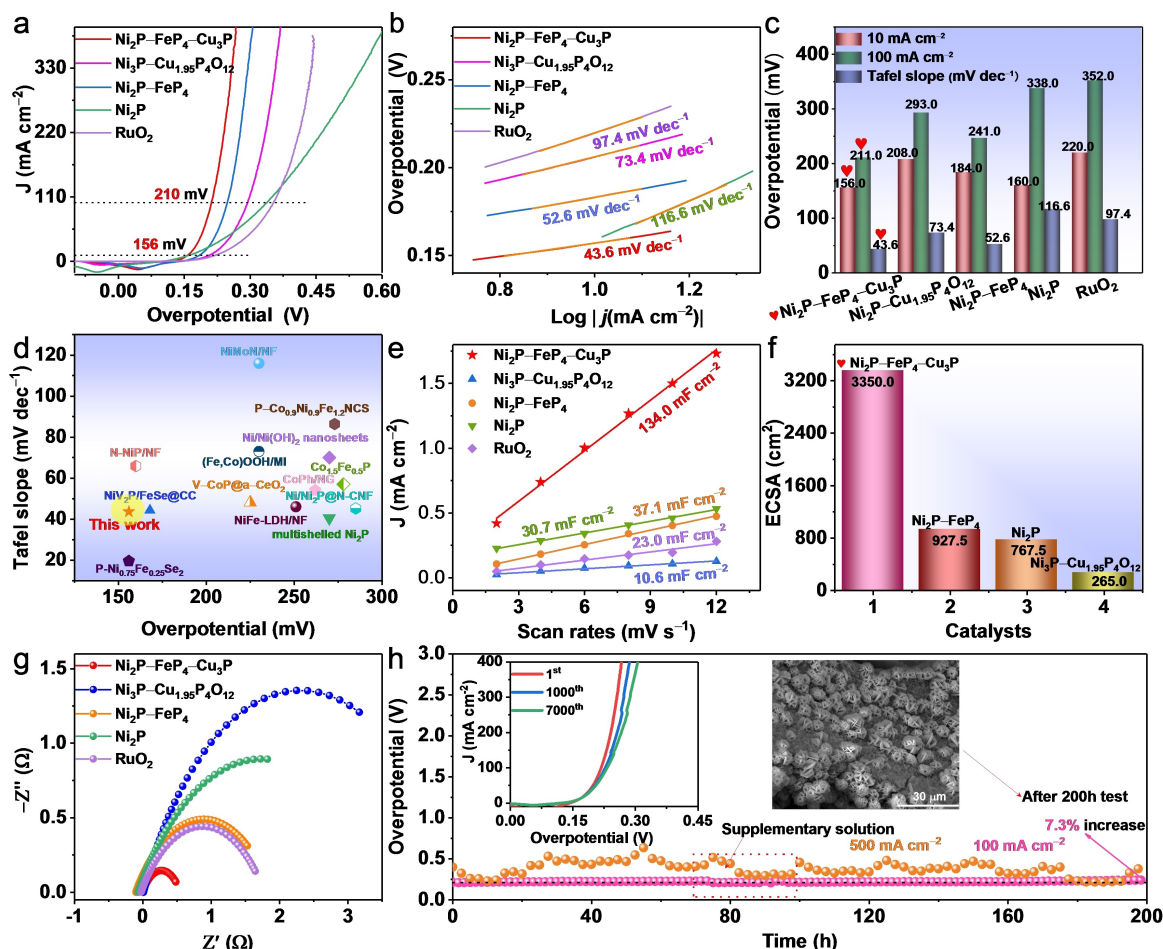
ChemSusChem

Research Article
doi.org/10.1002/cssc.202401872

Chemistry
Europe
European Chemical
Societies Publishing

Figure 4. (a) LSV polarization curves, (b) Tafel slopes, and (c) summary of overpotentials (at 10 and 200 mA cm^{-2}) and Tafel slopes of comparable catalysts in 1.0 M KOH. (d) Comparison of overpotential (at 10 mA cm^{-2}) and Tafel slopes for various state-of-the-art OER catalysts. (e) C_{dl}, (f) summary of ECSA, and (g) electrochemical impedance spectroscopy of designed catalysts. (h) Stability of the Ni$_2$P-FeP$_4$-Cu$_3$P/NF catalyst for OER (the inset shows the corresponding LSV curves at different cycles; the image displays the morphology of the Ni$_2$P-FeP$_4$-Cu$_3$P/NF after stability).

electrolyte, the Ni$_2$P-FeP$_4$-Cu$_3$P/NF$^{(+)}$||Pt/C$^{(-)}$ system requires a voltage of 1.47 V, which is notably lower than the 1.53 V required by the commercial RuO$_2^{(+)}$||Pt/C$^{(-)}$ system (inset Figure 5b). As depicted in Figure 5b, the Ni$_2$P-FeP$_4$-Cu$_3$P/NF$^{(+)}$||Pt/C$^{(-)}$ electrolyzer demonstrates exceptional efficiency, requiring only 1.73 and 1.85 V cell voltage to achieve high current densities of 400 and 800 mA cm^{-2}, respectively. This performance surpasses that of the commercial RuO$_2^{(+)}$||Pt/C$^{(-)}$ electrolyzer, which requires 1.97 and 2.07 V to reach comparable current densities. Further comparisons are presented in Figure 5c and Table S2, showcasing the Ni$_2$P-FeP$_4$-Cu$_3$P/NF$^{(+)}$||Pt/C$^{(-)}$ system's superior catalytic performance relative to other reported noble metal-free electrocatalysts. Owing to its hydrophilic surface properties and exceptional corrosion resistance, the Ni$_2$P-FeP$_4$-Cu$_3$P/NF$^{(+)}$||Pt/C$^{(-)}$ system also demonstrated stable operation for more than 60 h (Figure 5d), even under industrial-level current densities of 500 mA cm^{-2}, albeit with some fluctuations. This stability and efficiency highlight its potential for practical applications in water electrolysis, particularly in settings requiring high durability and efficiency.

Dynamic Transformation Analysis

Electrochemical impedance spectroscopy (EIS) serves as an effective method for obtaining insights into the adsorption and desorption kinetics of reactants on the electrode surface.[70] As shown in Figures 6a and S16a and b, the Nyquist plots from impedance measurements for OER process on Ni$_2$P-FeP$_4$-Cu$_3$P/NF, Ni$_3$P-Cu$_{1.95}$P$_4$O$_{12}$/NF, and Ni$_2$P-FeP$_4$/NF in 1.0 M KOH, ranging from an open circuit potential (OCP) to 1.50 V, reveal significant insights. The plots show large curved arcs in the low overpotential region, which notably shrink in the middle and high potential zones, suggesting enhanced kinetics and reactant adsorption as the potential increases. To better understand this behavior, the Nyquist plots are fitted with equivalent circuit diagrams (Figures S16 and S17), focusing on key parameters like the charge transfer resistance (R_{ct}) and the double-layer capacitance (C_{dl}). The R_{ct} represents the resistance against the adsorption of oxygen-containing reactants on the catalyst surface, while C_{dl} reflects charge transfer kinetics. Therefore, understanding the behavior of key oxo-species at the electrode/electrolyte interface through the analysis of adsorption
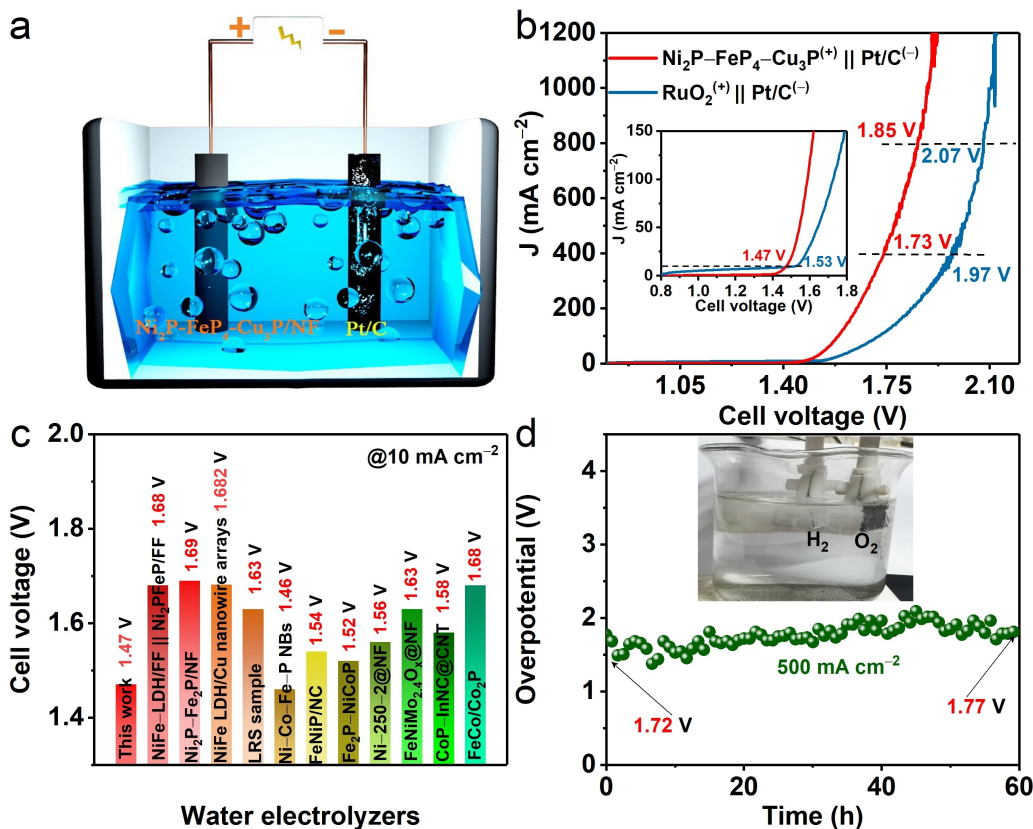
ChemSusChem

Research Article
doi.org/10.1002/cssc.202401872

Chemistry
Europe
European Chemical
Societies Publishing

Figure 5. (a) Schematic diagram of overall water splitting in the two-electrode system. (b) LSV curves of overall water splitting for Ni$_2$P-FeP$_4$-Cu$_3$P/NF$^{(+)}$||Pt/C$^{(-)}$ and RuO$_2^{(+)}$||Pt/C$^{(-)}$ in 1.0 M KOH. (c) Comparison the cell voltage of Ni$_2$P-FeP$_4$-Cu$_3$P/NF at 10 mA cm^{-2} with recently reported catalysts. (d) Chronopotentiometry test at 500 mA cm^{-2}.
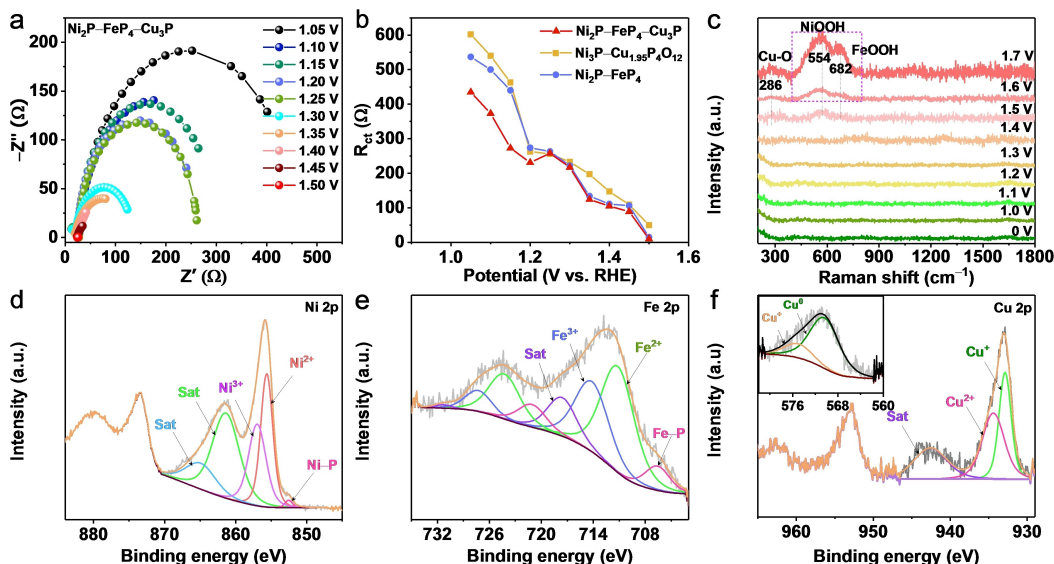

Figure 6. (a) Nyquist plots for the Ni$_2$P-FeP$_4$-Cu$_3$P/NF at different applied potentials in 1.0 M KOH. (b) Response of the ion adsorption-resistance (R$_{ct}$) at different potentials for various electrocatalysts. (c) Electrochemical in situ Raman spectra of the Ni$_2$P-FeP$_4$-Cu$_3$P/NF in the potential range of 0–1.70 V (vs. RHE). (d) Ni 2p, (e) Fe 2p, and (f) Cu 2p XPS spectra of the Ni$_2$P-FeP$_4$-Cu$_3$P/NF after OER stability (the inset shows Cu LMM Auger spectrum).

resistance (R$_{ct}$) is crucial for optimizing reaction processes. The alterations in R$_{ct}$, as depicted in Figure 6b, show that Ni$_2$P-FeP$_4$-Cu$_3$P/NF exhibits a lower R$_{ct}$ compared to Ni$_3$P-Cu$_{1.95}$P$_4$O$_{12}$/NF and Ni$_2$P-FeP$_4$/NF, indicating faster adsorption kinetics of critical

oxygen-containing reactive intermediates during the OER process. The notably rapid decrease in R$_{ct}$ for Ni$_2$P-FeP$_4$-Cu$_3$P/NF within the range of 1.1 V further underscores the swift adsorption of oxygen species at lower driving potentials,

resulting in the accumulation of key oxygen-containing reactive intermediates over the active hetero Ni_2P-FeP_4-Cu_3P/NF sites.[72]

In-situ Raman spectroscopy was employed to meticulously monitor the structural evolution of the precatalysts and to investigate the nature of the reconstructed active species under OER conditions.[73] In-situ Raman was used to track the transformation mechanism of Ni_2P-FeP_4-Cu_3P/NF during the OER process within the potential range of 1.0–1.7 V (vs. RHE, 1.0 M KOH), with a potential interval of 0.1 V (Figure 6c). At 0 V, the Raman spectrum represents the baseline data with no voltage applied. Upon increasing the potential to 1.4 V, two distinct peaks at 554 and 682 cm^{-1} emerge, corresponding to NiOOH and δ-FeOOH, respectively, indicating their role as active centers during OER.[74] Additionally, the peak at 286 cm^{-1} related to Cu—O suggests oxidation of Cu during OER.[77] These findings confirm that during the OER, Ni_2P-FeP_4-Cu_3P/NF undergoes surface reconstruction with in-situ formed NiOOH and δ-FeOOH acting as the active centers for OER.[76, 78]

Further analysis of the high-resolution XPS spectra of Ni_2P-FeP_4-Cu_3P/NF post-OER stability (Figure 6d–f) revealed a significant increase in the area ratio of high-valence states of Ni^{3+}, Fe^{3+}, and Cu^{2+} (Ni^{3+}/Ni^{2+} increased from 0.386 to 0.879, Fe^{3+}/Fe^{2+} from 0.854 to 1.554, and Cu^{2+}/Cu^+ from 0.445 to 1.120). The XPS spectra of Ni_2P-FeP_4-Cu_3P/NF after the OER tests confirmed that the Ni—P, Fe—P, and Cu—P doublets were replaced by those corresponding to Ni—O, Fe—O, and Cu—O. This indicates that the true active species for the OER are Ni, Fe, and Cu in their oxidized forms. This analysis, coupled with the presence of P—M bonds in high-resolution P 2p (Figure S18) indicates that metal hydroxide oxides/phosphides are the main active sites during the OER.[8, 13, 79]

The outstanding OER performance of the Ni_2P-FeP_4-Cu_3P/NF can be attributed to several key factors. Firstly, the flower-like structure provides a high specific surface area, which exposes more active sites and facilitates both electrolyte diffusion and gas release.[80] Secondly, the superhydrophilicity of the catalyst ensures close contact between the electrolytes and active sites, accelerating charge transfer and enhancing reaction kinetics.[49] Thirdly, the rich Fe defects in the Ni_2P-FeP_4-Cu_3P/NF catalyst improve conductivity and hydrophilicity, speeding up electron transfer and enhancing OER catalytic activity. Lastly, the synergistic effect of the abundant grain boundaries formed by the ternary metal phosphides optimizes the electronic structure of Ni_2P-FeP_4-Cu_3P/NF. In combination with the high-valence metal hydroxyl oxides generated during OER, these grain boundaries serve as true active sites, lowering the activation energy for oxygen-containing intermediates and boosting overall OER performance.[82]

Conclusions

The Ni_2P-FeP_4-Cu_3P/NF catalyst has shown remarkable efficiency in OER, significantly outperforming traditional catalysts like RuO_2 by achieving lower overpotentials of 156 mV and 210 mV at current densities of 10 and 100 mA cm^{-2}, respectively. Kinetic studies reveal its rapid OER kinetics, evidenced by a Tafel slope

of 43.6 mV dec^{-1}, and electrochemical impedance spectroscopy indicates it has the lowest charge transfer resistance among tested materials. Long-term stability tests further demonstrate its industrial viability, with the catalyst maintaining high activity over 200 h under a constant current density of 500 mA cm^{-2}. In-situ Raman spectroscopy and post-OER X-ray photoelectron spectroscopy confirm structural resilience and the formation of active centers like NiOOH and δ-FeOOH under operational conditions. Moreover, the synergistic effect of Fe and Cu integration into the Ni_2P matrix enhances the overall catalytic activity, with high-valence metal oxides and phosphides identified as the primary active sites during OER. These attributes make Ni_2P-FeP_4-Cu_3P/NF a promising alternative to noble metal-based catalysts for water electrolysis applications, offering a blend of high efficiency, superior stability, and enhanced kinetic properties.

Experimental Sections

Materials

Iron (III) nitrate nonahydrate ($Fe(NO_3)_3 \cdot 9H_2O$, 99%, Aladdin), copper (II) nitrate trihydrate ($Cu(NO_3)_2 \cdot 3H_2O$, 99%, Aladdin), urea ($CO(NH_2)_2$, 99.0%, Aladdin), ammonium fluoride (NH_4F, 96.0%, Aladdin), sodium hypophosphite monohydrate ($NaH_2PO_2 \cdot H_2O$, 99%, Aladdin), nitric acid (HNO_3, 65%~68%, Xilong), potassium hydroxide (KOH, 90%, Macklin), ethanol (C_2H_5OH, 99.7%, Xilong), Nafion (5 wt%, Alfa Aesar), Pt/C (20 wt% Pt, Sinero), nickel foam (NF) used as a substrate was obtained from Suzhou Sinero Technology Co, Ltd (with a thickness of 1.6 mm). RuO_2 powder was prepared by directly annealing $RuCl_3 \cdot 3H_2O$ (37%, Inno-chem) at 400 °C in air. All chemicals were used as received without further purification.

Synthesis of NiFeCu/NF

A piece (1.5 cm×3.5 cm) of nickel foam (NF) was ultrasonicated with 0.5 M H_2SO_4, ethanol, and deionized water, respectively, for 15 min to remove impurities from the NF surface. Subsequently, 1.25 mmol $Fe(NO_3)_3 \cdot 9H_2O$, 0.6 mmol $Cu(NO_3)_2 \cdot 3H_2O$, 4 mmol NH_4F, and 4.5 mmol $CO(NH_2)_2$ were dissolved in 40 mL deionized water to form a uniform solution under magnetic agitation at room temperature. Then the HNO_3 aqueous solution was slowly added to adjust the pH value of the above-prepared solution (pH = 2). After stirring the solution continuously for 30 min, the above treated NF was transferred together with the solution to a Teflon-lined stainless-steel autoclave (100 mL) and heated in an electric furnace at 120 °C for 12 h and then cooled naturally to room temperature. The obtained product (named NiFeCu/NF) was washed several times with ethanol and deionized water and then dried at 60 °C for 3 h.

NH_4F functions as an etching agent in catalyst synthesis, releasing active fluoride species (HF_2^- and NH_4^+) through hydrolysis. These species etch metal surfaces and enhance catalytic performance. However, fluoride ions are typically removed due to multiple washings during synthesis, as indicated by the absence of F in EDX and XPS spectra.

Synthesis of Ni_2P-FeP_4-Cu_3P/NF

$NaH_2PO_2 \cdot H_2O$ (1.0 g) and pre-prepared NiFeCu/NF were respectively placed upstream and downstream of the same tube furnace. The tube furnace was slowly heated to 350 °C for 120 min with a

ChemSusChem

Research Article
doi.org/10.1002/cssc.202401872

Chemistry
Europe
European Chemical
Societies Publishing

heating rate of $5\,°C\,min^{-1}$ in N_2 atmosphere to obtain $Ni_2P\text{-}FeP_4\text{-}Cu_3P/NF$.

In addition, we limited the total amount of metallic Fe to 1.25 mmol and made a series of proportional adjustments by changing the amount of Cu metal. The synthesis method was the same for all variants, and the catalysts obtained were named $Ni_2P\text{-}FeP_4\text{-}Cu_3P\text{-}0.2/NF$, $Ni_2P\text{-}FeP_4\text{-}Cu_3P\text{-}0.4/NF$, $Ni_2P\text{-}FeP_4\text{-}Cu_3P\text{-}0.8/NF$, and $Ni_2P\text{-}FeP_4\text{-}Cu_3P\text{-}1.0/NF$. We synthesized other catalysts in the same way, differing only in the pH adjustment of the solution. The pH values were adjusted to pH = 1, pH = 3, pH = 4, and pH = 5, respectively. The catalysts obtained were labeled according to the pH of the solution: $Ni_2P\text{-}FeP_4\text{-}Cu_3P/NF\text{-}pH = 1$, $Ni_2P\text{-}FeP_4\text{-}Cu_3P/NF\text{-}pH = 3$, $Ni_2P\text{-}FeP_4\text{-}Cu_3P/NF\text{-}pH = 4$, and $Ni_2P\text{-}FeP_4\text{-}Cu_3P/NF\text{-}pH = 5$.

In comparison, $Ni_2P\text{-}FeP_4/NF$, $Ni_3P\text{-}Cu_{1.95}P_4O_{12}/NF$, and NF—P were synthesized in a manner similar to $Ni_2P\text{-}FeP_4\text{-}Cu_3P/NF$.

Synthesis of RuO_2/NF and 20 wt% Pt/C/NF Electrodes

RuO_2 (2 mg) and 20 wt% Pt/C were dispersed into a solution containing 200 μL deionized water, 200 μL ethanol and 10 μL of 5 wt% Nafion solution. The mixture was sonicated for 30 min to obtain a homogeneous solution. This solution was then drop-coated onto a clean NF (1 cm×1 cm) and dried in air.

Electrochemical Measurements

All electrochemical tests of the catalysts synthesized in this experiment were carried out on a Biologic VMP3 electrochemical workstation. The workstation uses a standard three-electrode system with an electrolyte solution of 1.0 M KOH (pH = 13.5). The working electrode for electrochemical testing was a prepared NF-based catalyst (1 cm×1 cm), the counter electrode was a graphite plate, and the reference electrode was a standard calomel electrode (SCE). Linear sweep voltammetry, which was used to measure the electrochemical properties of the catalysts was reverse scanned and carried out in the range of 1.2–0 V (vs. SCE) at a sweep rate of $0.5\,mV\,s^{-1}$. Electrochemical impedance spectroscopy (EIS) measurements were determined at a voltage of 0.5 V (vs. SCE) over a frequency range of 300 kHz to 10 mHz, and finally the EIS data were fitted with ZSimDemo software. The electrochemical surface area (ECSA) was determined from the double-layer capacitance (C_{dl}), which in turn was obtained by cyclic voltammetry (CV) characterization The CV characterization was measured in the non-Faraday interval voltage range of 0.1–0.2 V (vs. SCE) at scan rates of 2, 4, 6, 8, 10, and $12\,mV\,s^{-1}$ respectively. The formula for calculating the C_{dl} was: $C_{dl} = (j_a - j_c)/(2 \times v)$, where j_a and j_c correspond to the anode and cathode current densities respectively, and v represents the scanning rate. The ECSA was calculated as: $ECSA = C_{dl}/C_s$, where the C_s value was generally between 20 and $60\,\mu F\,cm^{-2}$, with an average of $40\,\mu F\,cm^{-2}$. The stability of the catalyst was measured by chronopotentiometry at a current density of 10 and $100\,mA\,cm^{-2}$ for an extended time period. The overall water splitting tests were carried out in a 1.0 M KOH electrolyte with potentials ranging from 0–2.5 V and a scan rate of $5\,mV\,s^{-1}$. Experimentally measured potentials were converted to the RHE scale using the Nernst equation: E (vs. RHE) $= E_{SCE} + 0.059 \times pH + 0.0.241$ V and corrected with 100% iR according to equation.

In situ Raman spectroscopy experiments require a specific Raman spectrometer (InVia Qontor, Renishaw) equipped with an in situ test cell (Gaoss Union C031-1) for experimental determination in 1.0 M KOH solution. The as-prepared catalyst was used as the working electrode, the carbon rod as the counter electrode and the Ag/AgCl electrode as the reference electrode. The laser excitation wavelength was set at 785 nm and the exposure time for each spectral recording was 10 min. The evolution of the catalyst was monitored by collecting Raman spectra at a constant potential of 1.0–1.7 V (vs. RHE).

In situ EIS measurements: In situ characterization with tandem electrochemical operation was carried out by maintaining the potential at 0.95–1.45 V (vs. RHE) for 10 min to obtain the surface chemical composition and structural information of the materials. EIS tests were performed at different potentials in the frequency range of 300 kHz to 10 mHz.

Conflict of Interests

The authors declare that they have no known competing financial interests or personal relationships that could have appeared to influence the work reported in this paper.

Data Availability Statement

Research data are not shared.

[1] X. Pan, M. Yan, Q. Liu, X. Zhou, X. Liao, C. Sun, J. Zhu, C. McAleese, P. Couture, M. K. Sharpe, R. Smith, N. Peng, J. England, S. C. E. Tsang, Y. Zhao, L. Mai, *Nat. Commun.* **2024**, *15*, 3354.

[2] P. De Luna, C. Hahn, D. Higgins, S. A. Jaffer, T. F. Jaramillo, E. H. Sargent, *Science* **2019**, *364*, 350–364.

[3] G. Singh, K. Ramadass, V. D. B. C. DasiReddy, X. Yuan, N. Sik Ok, N. Bolan, X. Xiao, T. Ma, A. Karakoti, J. Yi, A. Vinu, *Prog. Mater. Sci.* **2023**, *135*, 101104.

[4] L. Magnier, G. Cossard, V. Martin, C. Pascal, V. Roche, E. Sibert, I. Shchedrina, R. Bousquet, V. Parry, M. Chatenet, *Nat. Mater.* **2024**, *23*, 252–261.

[5] G. Li, G. Han, L. Wang, X. Cui, N. K. Moehring, P. R. Kidambi, D.-e. Jiang, Y. Sun, *Nat. Commun.* **2023**, *14*, 525.

[6] Z. W. Seh, J. Kibsgaard, C. F. Dickens, I. Chorkendorff, J. K. Nørskov, T. F. Jaramillo, *Science* **2017**, *355*, 4998.

[7] H. Lei, Q. Wan, S. Tan, Z. Wang, W. Mai, *Adv. Mater.* **2023**, *35*, 2208209.

[8] X. Li, J. Zhou, C. Liu, L. Xu, C. Lu, J. Yang, H. Pang, W. Hou, *Appl. Catal., B* **2021**, *298*, 120578.

[9] L. Zhang, Z. Wang, J. Zhang, Z. Lin, Q. Zhang, W. Zhong, G. Wu, *Nano Res.* **2023**, *16*, 6552–6559.

[10] T. L. Luyen Doan, D. T. Tran, D. C. Nguyen, H. Tuan Le, N. H. Kim, J. H. Lee, *Appl. Catal., B* **2020**, *261*, 118268.

[11] E. Cao, Z. Chen, H. Wu, P. Yu, Y. Wang, F. Xiao, S. Chen, S. Du, Y. Xie, Y. Wu, Z. Ren, *Angew. Chem., Int. Ed.* **2020**, *59*, 4154–4160.

[12] H. Feng, L. Tang, G. Zeng, J. Yu, Y. Deng, Y. Zhou, J. Wang, C. Feng, T. Luo, B. Shao, *Nano Energy* **2020**, *67*, 104174.

[13] M. Li, J. Wang, X. Guo, J. Li, Y. Huang, S. Geng, Y. Yu, Y. Liu, W. Yang, *Appl. Surf. Sci.* **2021**, *536*, 147909.

[14] Y. Feng, C. Xu, E. Hu, B. Xia, J. Ning, C. Zheng, Y. Zhong, Z. Zhang, Y. Hu, *J. Mater. Chem. A* **2018**, *6*, 14103–14111.

[15] L. Yu, J. Zhang, Y. Dang, J. He, Z. Tobin, P. Kerns, Y. Dou, Y. Jiang, Y. He, S. L. Suib, *ACS Catal.* **2019**, *9*, 6919–6928.

[16] H. Wu, B. Liu, Y. Zhang, F. Li, J. Liu, L. Zhao, P. Zhang, L. Gao, *J. Mater. Sci.* **2024**, *59*, 6270–6284.

[17] H. Jiang, Z. Zhao, G. Li, M. Wang, P. Chen, X. Liu, X. Tu, Y. Hu, Z. Shen, Y. Wu, *Adv. Sci.* **2024**, *11*, 2306919.

[18] Z. Yang, X. Feng, R. Liu, H. Zhang, P. Peng, W. Wu, Z. Li, Z. Hou, K. Huang, *J. Taiwan Inst. Chem. Eng.* **2023**, *147*, 104916.

[19] L. Yan, B. Zhang, J. Zhu, Y. Li, P. Tsiakaras, P. Kang Shen, *Appl. Catal., B* **2020**, *265*, 118555.

[20] J. Ge, S. Diao, J. Jin, Y. Wang, X. Zhao, F. Zhang, X. Lei, *Inorg. Chem. Front.* **2023**, *10*, 3515–3524.

[21] R. Xiang, Y. Duan, L. Peng, Y. Wang, C. Tong, L. Zhang, Z. Wei, *Appl. Catal., B* **2019**, *246*, 41–49.

[22] P. Ding, C. Meng, J. Liang, T. Li, Y. Wang, Q. Liu, Y. Luo, G. Cui, A. M. Asiri, S. Lu, X. Sun, *Inorg. Chem.* **2021**, *60*, 12703–12708.

[23] A. Li, L. Zhang, F. Wang, L. Zhang, L. Li, H. Chen, Z. Wei, *Appl. Catal., B* **2022**, *310*, 121353.

[24] T. Zhou, Y. Ma, H. Feng, Y. Lu, G. Che, C. Liu, Y. Lan, *Adv. Funct. Mater.* **2024**, *17*, 2409396.

[25] X. Yang, B. Ouyang, L. Zhao, Q. Shen, G. Chen, Y. Sun, C. Li, K. Xu, *J. Am. Chem. Soc.* **2023**, *145*, 27010–27021.

[26] X. Qiao, H. Kang, Y. Li, K. Cui, X. Jia, X. Wu, W. Qin, *Appl. Catal., B* **2022**, *305*, 121034.

[27] W. Cheng, H. Zhang, X. Zhao, H. Su, F. Tang, J. Tian, Q. Liu, *J. Mater. Chem. A* **2018**, *6*, 9420–9427.

[28] D. Yan, Y. Li, J. Huo, R. Chen, L. Dai, S. Wang, *Adv. Mater.* **2017**, *29*, 1606459.

[29] Z. Wu, Y. Zhao, H. Wu, Y. Gao, Z. Chen, W. Jin, J. Wang, T. Ma, L. Wang, *Adv. Funct. Mater.* **2021**, *31*, 2010437.

[30] X. Chen, L. Chen, C. Chen, D. Shi, J. Song, Y. Qin, X. Wang, M. M. Amjad, D. Sun, B. Sun, K. Zhang, *Adv. Mater.* **2024**, *36*, 2401110.

[31] Y. Luo, Z. Zhang, M. Chhowalla, B. Liu, *Adv. Mater.* **2022**, *34*, 2108133.

[32] T. Liu, X. Yu, Y. Wu, X. Chu, W. Jiang, B. Liu, C. Liu, G. Che, *Small Methods* **2024**, *310*, 2401082.

[33] S. Chen, Y. Zhuo, X. Wang, S. Li, J. Lu, D. Liu, H. Pan, Z. Wang, *Coord. Chem. Rev.* **2024**, *510*, 215832.

[34] H. Chen, R. Ding, B.-W. Liu, F.-R. Zeng, H.-B. Zhao, *Small* **2024**, *20*, 2306274.

[35] A. A. Dubale, C.-J. Pan, A. G. Tamirat, H.-M. Chen, W.-N. Su, C.-H. Chen, J. Rick, D. W. Ayele, B. A. Aragaw, J.-F. Lee, Y.-W. Yang, B.-J. Hwang, *J. Mater. Chem. A* **2015**, *3*, 12482–12499.

[36] A. Y. Faid, A. O. Barnett, F. Seland, S. Sunde, *Electrochim. Acta* **2020**, *361*, 137040.

[37] W. Lai, L. Ge, H. Li, Y. Deng, B. Xu, B. Ouyang, E. Kan, *Int. J. Hydrogen Energy* **2021**, *46*, 26861–26872.

[38] Z. Zhou, Y. Kong, H. Tan, Q. Huang, C. Wang, Z. Pei, H. Wang, Y. Liu, Y. Wang, S. Li, X. Liao, W. Yan, S. Zhao, *Adv. Mater.* **2022**, *34*, 2106541.

[39] J. Zhang, D. Zeng, Q. Zhu, J. Wu, Q. Huang, C. Xie, *J. Phys. Chem. C* **2016**, *120*, 3936–3945.

[40] Z. Nie, C. Sui, X. Xie, S.-Q. Ni, L. Kong, Y. Wang, J. Zhan, *Appl. Catal., B* **2024**, *347*, 123819.

[41] B. Liu, Y. Wang, H.-Q. Peng, R. Yang, Z. Jiang, X. Zhou, C.-S. Lee, H. Zhao, W. Zhang, *Adv. Mater.* **2018**, *30*, 1803144.

[42] J. Chen, Y. Zhang, Z. Zhang, D. Hou, F. Bai, Y. Han, C. Zhang, Y. Zhang, J. Hu, *J. Mater. Chem. A* **2023**, *11*, 8540–8572.

[43] X. Guo, J. Mao, R. Zhou, *J. Power Sources* **2017**, *371*, 119–128.

[44] K. Zhuo, C. Y. An, P. K. Kannan, N. Seo, Y.-S. Park, C.-H. Chung, *Korean J. Chem. Eng.* **2017**, *34*, 1483–1489.

[45] H. Cao, X. Li, Y. Chen, M. Gong, J. Wang, *J. Rare Earths* **2012**, *30*, 871–877.

[46] S. Wen, J. Huang, T. Li, W. Chen, G. Chen, Q. Zhang, X. Zhang, Q. Qian, K. Ostrikov, *Appl. Catal., B* **2022**, *316*, 121678.

[47] J. Xu, J. Li, D. Xiong, B. Zhang, Y. Liu, K.-H. Wu, I. Amorim, W. Li, L. Liu, *Chem. Sci.* **2018**, *9*, 3470–3476.

[48] J. Lin, Y. Yan, C. Li, X. Si, H. Wang, J. Qi, J. Cao, Z. Zhong, W. Fei, J. Feng, *Nano-Micro Lett.* **2019**, *11*, 55.

[49] L. Wu, L. Yu, F. Zhang, B. McElhenny, D. Luo, A. Karim, S. Chen, Z. Ren, *Adv. Funct. Mater.* **2021**, *31*, 2006484.

[50] D. Zhou, S. Wang, Y. Jia, X. Xiong, H. Yang, S. Liu, J. Tang, J. Zhang, D. Liu, L. Zheng, Y. Kuang, X. Sun, B. Liu, *Angew. Chem., Int. Ed.* **2019**, *58*, 736–740.

[51] Y. Xing, J. Ku, W. Fu, L. Wang, H. Chen, *Chem. Eng. J.* **2020**, *395*, 125149.

[52] M. Li, J. Sun, X. Zhou, H. Yao, J. Cong, Y. Li, G. Chen, *Appl. Catal., B* **2023**, *322*, 122096.

[53] J. Tian, Q. Liu, N. Cheng, A. M. Asiri, X. Sun, *Angew. Chem., Int. Ed.* **2014**, *53*, 9577–9581.

[54] M. Guo, Z. Huang, Y. Qu, L. Wang, H. Li, T. T. Isimjan, X. Yang, *Appl. Catal., B* **2023**, *320*, 121991.

[55] G. Li, J. Tu, M. Wang, S. Jiao, *J. Mater. Chem. A* **2019**, *7*, 8368–8375.

[56] M. Qu, F.-Q. Zhang, D.-H. Wang, H. Li, J.-J. Hou, X.-M. Zhang, *Angew. Chem. Int. Ed.* **2020**, *59*, 6507–6512.

[57] S. Laing, K. Gracie, K. Faulds, *Chem. Soc. Rev.* **2017**, *46*, 6074–6074.

[58] K. Xu, H. Ding, M. Zhang, M. Chen, Z. Hao, L. Zhang, C. Wu, Y. Xie, *Adv. Funct. Mater.* **2017**, *29*, 1606980.

[59] W.-K. Chong, B.-J. Ng, Y. J. Lee, L.-L. Tan, L. K. Putri, J. Low, A. R. Mohamed, S.-P. Chai, *Nat. Commun.* **2023**, *14*, 7676.

[60] Y. Si, Z. Dong, L. Jiang, *ACS Cent. Sci.* **2018**, *4*, 1102–1112.

[61] Z. Wu, Y. Zhao, H. Wu, Y. Gao, Z. Chen, W. Jin, J. Wang, T. Ma, L. Wang, *Adv. Funct. Mater.* **2021**, *31*, 2010437.

[62] M. Liu, Z. Sun, S. Li, X. Nie, Y. Liu, E. Wang, Z. Zhao, *J. Mater. Chem. A* **2021**, *9*, 22129–22139.

[63] Q. Mo, W. Zhang, L. He, X. Yu, Q. Gao, *Appl. Catal., B* **2019**, *244*, 620–627.

[64] T. Li, Y. Lv, J. Su, Y. Wang, Q. Yang, Y. Zhang, J. Zhou, L. Xu, D. Sun, Y. Tang, *Adv. Sci.* **2017**, *4*, 1700226.

[65] Y. Hu, Z. Luo, M. Guo, J. Dong, P. Yan, C. Hu, T. T. Isimjan, X. Yang, *Chem. Eng. J.* **2022**, *435*, 134795.

[66] H. Liu, X. Ma, Y. Rao, Y. Liu, J. Liu, L. Wang, M. Wu, *ACS Appl. Mater. Interfaces* **2018**, *10*, 10890–10897.

[67] X. Huang, X. Xu, X. Luan, D. Cheng, *Nano Energy* **2020**, *68*, 104332.

[68] M.-I. Jamesh, M. Harb, *J. Energy Chem.* **2021**, *56*, 299–342.

[69] J. Nai, X. W. Lou, *Adv. Mater.* **2019**, *31*, 1706825.

[70] Z. Xiao, Y.-C. Huang, C.-L. Dong, C. Xie, Z. Liu, S. Du, W. Chen, D. Yan, L. Tao, Z. Shu, G. Zhang, H. Duan, Y. Wang, Y. Zou, R. Chen, S. Wang, *J. Am. Chem. Soc.* **2020**, *142*, 12087–12095.

[71] W. Zhou, H. Su, Z. Wang, F. Yu, W. Wang, X. Chen, Q. Liu, *J. Mater. Chem. A* **2021**, *9*, 1127–1133.

[72] H. Su, W. Zhou, W. Zhou, Y. Li, L. Zheng, H. Zhang, M. Liu, X. Zhang, X. Sun, Y. Xu, F. Hu, J. Zhang, T. Hu, Q. Liu, S. Wei, *Nat. Commun.* **2021**, *12*, 6118.

[73] B. Li, J. Zhao, Y. Wu, G. Zhang, H. Wu, F. Lyu, J. He, J. Fan, J. Lu, Y. Y. Li, *Small* **2023**, *19*, 2301715.

[74] J. Huang, Y. Li, Y. Zhang, G. Rao, C. Wu, Y. Hu, X. Wang, R. Lu, Y. Li, J. Xiong, *Angew. Chem., Int. Ed.* **2019**, *58*, 17458–17464.

[75] Y. Shi, Y. Du, W. Zhou, C. Wang, S. Lu, S. Lu, B. Zhang, *Angew. Chem., Int. Ed.* **2020**, *59*, 22470–22474.

[76] M. W. Louie, A. T. Bell, *J. Am. Chem. Soc.* **2013**, *135*, 12329–12337.

[77] R. Govindhan, B. Karthikeyan, *J. Phys. Chem. Solids* **2017**, *111*, 123–134.

[78] P. Yan, Q. Liu, H. Zhang, L. Qiu, H. B. Wu, X.-Y. Yu, *J. Mater. Chem. A* **2021**, *9*, 15586–15594.

[79] J. Yan, L. Kong, Y. Ji, J. White, Y. Li, J. Zhang, P. An, S. Liu, S.-T. Lee, T. Ma, *Nat. Commun.* **2019**, *10*, 2149.

[80] X. Liu, S. Deng, P. Liu, J. Liang, M. Gong, C. Lai, Y. Lu, T. Zhao, D. Wang, *Sci. Bull.* **2019**, *64*, 1675–1684.

[81] N. Chen, S. Che, H. Liu, G. Li, N. Ta, F. Jiang Chen, B. Jiang, N. Wu, Z. Li, W. Yu, F. Yang, Y. Li, *J. Colloid Interface Sci.* **2023**, *638*, 582–594.

[82] M. Liu, L. Yang, T. Liu, Y. Tang, S. Luo, C. Liu, Y. Zeng, *J. Mater. Chem. A* **2017**, *5*, 8608–8615.

[83] G. Zhao, K. Rui, S. X. Dou, W. Sun, *J. Mater. Chem. A* **2020**, *8*, 6393–6405.